Atmospheric Carbon Dioxide Measurement from Aircraft and Comparison with OCO-2 and CarbonTracker Model Data

Qin Wang[1], Farhan Mustafa[1], Lingbing Bu[1], Shouzheng Zhu[1,2], Jiqiao Liu[2], Weibiao Chen[2]

5   [1]Collaborative Innovation Center on Forecast and Evaluation of Meteorological Disasters, Nanjing University of Information Science and Technology (NUIST), Nanjing, 210044, China
[2]Key Laboratory of Space Laser Communication and Detection Technology, Shanghai Institute of Optics and Fine Mechanics, Chinese Academy of Sciences, Shanghai 201800, China

Correspondence to: Lingbing Bu (lingbingbu@nuist.edu.cn)

10   **Abstract.** Accurate monitoring of the atmospheric carbon dioxide (CO_2) and its distribution is of great significance for studying the carbon cycle and predicting the future climate change. Compared to the ground observational sites, the airborne observations cover a wider area, and simultaneously observe a variety of surface types, which help in effectively monitoring the distribution of CO_2 sources and sinks. In this work, an airborne experiment was carried out in March 2019 over Shanhaiguan area, China (39-41N,119-121E). An Integrated Path Differential Absorption (IPDA) Light Detection and Ranging (LIDAR)
15   system and a commercial instrument, the Ultraportable Greenhouse Gas Analyzer (UGGA), were used installed on an aircraft to observe the CO_2 distribution over various surface types. The Pulse Integration Method (PIM) algorithm was used to calculate the Differential Absorption Optical Depth (DAOD) from the LIDAR data. The CO_2 column-averaged dry-air mixing ratio (XCO_2) was calculated over different types of surfaces including mountain, ocean and urban areas. The concentrations of the XCO_2 calculated from LIDAR measurements over ocean, mountain, and urban areas were 421.11, 427.67, and 430 ppm,
20   respectively. Moreover, through the detailed analysis of the data obtained from the UGGA, the influence of pollution levels on the CO_2 concentration was also studied. During the whole flight campaign, March 18 was heavily polluted with an Air Quality Index (AQI) of 175 and $PM_{2.5}$ of 131. The Aerosol Optical Depth (AOD) reported by a sun photometer installed at the Funning ground station was 1.28. Compared to the other days, the CO_2 concentration measured by UGGA at different heights was the largest on March 18 with an average value of 422.59 ppm, that was about 10 ppm higher than the measurements
25   recorded on March 16. Moreover, the vertical profiles of Orbiting Carbon observatory-2 (OCO-2) and CarbonTracker were also compared with the aircraft measurements. All the datasets showed a similar variation trend with some differences in their CO_2 concentrations, which proved the existence of a good agreement among them.

1 Introduction

Atmospheric carbon dioxide (CO_2) is the most important greenhouse gas, and it plays a significant role in hydrology, sea ice
30   melting, sea level rise, and atmospheric temperature changes (Mustafa et al., 2020; Santer et al., 2013; Stocker et al., 2013).

Since the industrial revolution, the increase in the anthropogenic activities have caused a significant rise in the CO_2 concentration, which is considered an important factor for climate change (Ballantyne et al., 2012; Dlugokencky Ed, 2016). Accurate measurement of atmospheric CO_2 and its spatiotemporal variation is crucial for estimating the distribution and dynamics of carbon sources and sinks at regional and global scales (Araki et al., 2010; Mustafa et al., 2021). There are several

35   ground-based stations such as the Total Carbon Column Observing Network (TCCON) sites and the stations within the Global Atmospheric Watch (GAW) network, which are monitoring the atmospheric CO_2 with great precision (Hedelius et al., 2017; Hungershoefer et al., 2010; Mendonca et al., 2019; Schultz et al., 2015). However, these observational sites are not sufficient to accurately monitoring the atmospheric CO_2 at regional and global scales due to their limited spatial coverage and uneven distribution (Kulawik et al., 2016). Previous studies suggested that the space-based instruments could provide the most

40   effective way to monitor the atmospheric CO_2 at regional and global scales with great spatiotemporal resolutions (Kong et al., 2019; Lindqvist et al., 2015). Since the past decade, several satellites have been launched which are dedicatedly monitoring the greenhouse gases including the atmospheric CO_2 and the methane (Crisp, 2015; Yokota et al., 2009). These satellites calculate the average atmospheric CO_2 concentrations in the path of sunlight reflected by the surface through spectrometers carried onboard. The measurements obtained from these satellites are vulnerable to the clouds and aerosols and much of the

45   data is screened out due to the contamination of clouds and aerosol content in the measurements. Greenhous gases Observing SATellite (GOSAT) and the OCO-2 were the first two CO_2 monitoring satellites which were successfully put into the orbit. Both of them measure the CO_2 optical depth with the bands centred around 1.6 and 2.0 μm, and O_2 with band A, centred around 0.76 μm (Kiel et al., 2019).

The IPDA LIDAR is also an effective tool to observe the atmospheric CO_2 and other atmospheric variables (Gong et al., 2020;

50   Xie et al., 2020; Zhu et al., 2020). Several studies have used the ground-based and airborne IPDA LIDAR systems to measure the atmospheric CO_2 (Ehret et al., 2008; Kawa et al., 2010). Moreover, the feasibility and the sensitivity analyses of the space-borne CO_2 monitoring LIDAR systems have also been carried out and the corresponding instruments have been put into use in several countries including the United States, China, and Germany (Abshire et al., 2013; Mao et al., 2018b, 2018a; Du et al., 2017; Liang et al., 2017; Amediek et al., 2017). Like the GOSAT and OCO-2, most of the IPDA LIDAR systems also

55   focus on the wavelengths of 1.6 and 2.0 μm to measure the atmospheric CO_2. The National Aeronautics and Space Administration (NASA) Goddard Space Flight centre developed a pulsed IPDA LIDAR instrument incorporating a HgCdTe Avalanche Photodiode detector (APD) and multiple-wavelength-locked laser to measure the XCO_2 and carried out its first airborne campaign in 2011 (Abshire et al., 2013). Later, the instrument was improved and the latest results from the airborne campaign carried out during 2014 and 2016 showed an accuracy of 0.8 ppm over a desert area (Abshire et al., 2018). The

60   measurements obtained from the IPDA LIDAR system were evaluated against in-situ instrument observations and the differences were within a range of 1 ppm. Another CO_2 monitoring double-pulsed, 2 μm IPDA LIDAR instrument developed by NASA Langley Research Centre carried out its airborne operation in 2014 to measure the atmospheric CO_2 (Refaat et al., 2016). The results showed a difference of 0.36% relative to the CO_2 mixing ratio measured by the National Oceanic and Atmospheric Administration (NOAA) flask sampling data (Yu et al., 2017). In addition, the German Research Space Centre

65 (GRSC) developed a 1.57 μm double-pulse IPDA LIDAR instrument and measured the atmospheric CO_2 concentration with great accuracy during their airborne campaign in 2015 (Amediek et al., 2017).

China significantly contributes to the global CO_2 emission mainly due to the strong anthropogenic activities (Mustafa et al., 2020). The northern China, in particular, Beijing-Tianjin-Hebei is the most populated region with the largest anthropogenic emissions in the world (Lei et al., 2017; Yang et al., 2019). Under the United Nations Framework Convention on Climate

70 Change (UNFCCC) 2015 Paris Climate Agreement, China pledged to reduce the CO_2 emission per unit gross domestic product (GDP) by 60-65% compared to 2005 levels, and peak carbon emission overall, by 2030 (UNFCC, 2015). It is crucial to measure the atmospheric CO_2 using precise and accurate instruments for monitoring of the CO_2 reduction progress and evaluation of how well specific policies are working. In this study, an airborne campaign was carried out during March 2019 to measure the atmospheric CO_2 using an IPDA LIDAR, and a commercial instrument Ultraportable Greenhouse Gas Analyzer (UGGA;

75 model 915-0011; Los Gatos Research, San Jose, CA, USA) over northeast China. The primary objective of the study was to evaluate the performance of a newly developed IPDA LIDAR instrument over different types of surfaces including water bodies, mountains and urban residential areas. In addition, the influence of pollution on the atmospheric CO_2 concentration was also studied using the measurement obtained from the UGGA installed on the aircraft. The details about observational site, flight campaign, and instruments are provided in Section 2. The results including the IPDA LIDAR measurements, UGGA

80 observations and their comparisons are discussed in Section 3.

2 Materials and Methods

2.1 Aircraft Instrumentation

The aircraft used in this experiment was a Yun-8, which was equipped with four turboprop engines. The cruise and the maximum speeds of the aircraft were 550 and 660 km h−1, respectively. The Atmospheric Carbon Dioxide LIDAR (ACDL)

85 conducted its first flight experiment during March 2019 over Shanhaiguan, China. The working wavelengths of the ACDL were 532, 1064, and 1572 nm, respectively. The 1572 nm channel was used for IPDA technique to measure the atmospheric CO_2, while 532 and 1064 nm channels were used to detect the aerosols and clouds. The aerosol and cloud optical parameters, such as the extinction coefficient, backscatter coefficient, LIDAR ratio and the Aerosol Optical Depth (AOD) are helpful in providing accurate inversion of CO_2 column concentration (Crisp et al., 2012; O'Dell et al., 2012). More detail about the

90 ACDL is described in our previous article (Zhu et al., 2020). The ACDL system used for the atmospheric CO_2 measurement is shown in Figure 1, and more detail about the main components of the system is provided in Table 1.

Table 1: The main parameters of the airborne dual-wavelength IPDA LIDAR system.

Parameters	Value	Parameters	Value
Online wavelength	1572.024 nm	Telescope diameter	150 mm
Offline wavelength	1572.085 nm	Field of view	1 mrad

Pulse energy(on/off)	6/3 mJ	Beam divergence	0.62 mrad
Pulse width(on/off)	17 ns	Emission optical efficiency	0.8955
Repetition frequency	30 Hz	Receiver optical efficiency	0.3797
Frequency stability	2.7 MHz	Data acquisition	125 MS/s

The ACDL consisted of a laser transmitter, an instrument control, an environmental control, and a LIDAR transceiver
subsystem. Figure 1(a) shows the transceiver system. It mainly included a laser, a telescope, a receiving system and an APD
detector, which were mounted in a pod outside the aircraft. Figure 1(b) shows the laser frequency monitoring and control
system, electronic control system and the data acquisition system of the equipment. These systems were installed inside the
aircraft and armoured optical fibres and cables were used to transmit the information to the instruments in the pod. An Inertial
Navigation System (INS) was also installed to record the attitude information of the aircraft during the flight. The real-time
altitude and position information of aircraft were acquired using a Global Positioning System (GPS) system. Figure 1(c) shows
the Aircraft Integrated Meteorological Measurement System (AIMMS). The AIMMS was installed to measure the atmospheric
temperature, pressure, relative humidity and other meteorological parameters during the flight. Figure 1(d) shows a commercial
instrument UGGA, that was installed in an unsealed cabin of the aircraft and a 1/4-inch Teflon pipe was used to connect it
with the external atmosphere. The UGGA used a laser absorption technology known as the off-axis Integrated Cavity Output
Spectroscopy (ICOS) to measure trace gas concentration in dry mole fraction with a high precision of <0.30 ppm for CO_2 and
<2 ppb for CH_4 (UGGA user manual; model 915-0011; Los Gatos Research, San Jose, CA, USA). More details about the
UGGA and ICOS spectroscopy are given in previous studies (Baer et al., 2002; Paul et al., 2001; Sun et al., 2020). Before the
flight experiment, the UGGA was calibrated against the standard gas, and the uncertainty was within 0.1 ppm.

2.2 Experimental Site

The airborne campaign was conducted from 11 – 19 March 2019. More detail about the flights is given in Table 2. Figure 2
shows the geolocation of the experimental site and path of the flight carried out on 14 March. In order to detect the changing
trend of atmospheric CO_2 concentration over various types of surfaces, the path of the flight was designed to observe the ocean,
urban residential and the mountain areas. The starting point of the flight was A, and the ending point was B. The flight path
covered a variety of surface types, including the ocean, the mountain, and the urban residential areas. The distribution of the
carbon sources and sinks in the study area can be more accurately distinguished through the detection of various surface types.
Figure 3 shows the flight altitude and the corresponding surface elevation information during the level flight period. The
altitude of the aircraft was measured by the GPS system. The height and the ground elevation were measured using the airborne
IPDA LIDAR. The altitude of the horizontal flight of the plane on March 14 was about 6.8 km. Moreover, the altitude
information about various types of surfaces is also shown in Figure 3.

Table 2: Details of flight on each day.

Date	Horizontal flight time	Flight Altitude (km)

11 March	10:26 - 14:43	5
14 March	10:18 - 12:06	6.8
16 March	10:34 - 12:46	7.8
18 March	10:21 – 14:18	4
19 March	10:21 – 14:05	5

2.3 Datasets

2.3.1 Aircraft Data

125 A variety of data were measured using the aircraft and incorporated in this study. The aircraft data included the ACDL data, in-situ data and the auxiliary data. The in-situ CO_2 dry-air mole fraction data was measured using the UUGA which was installed in an unsealed cabin of the aircraft. The auxiliary data included the inertial navigational and meteorological data. The inertial navigational data was measured using the INS, and the meteorological data was measured using the AIMMS, which was installed on the aircraft shell. In addition, a colour Complementary Metal Oxide Semiconductor (CMOS) camera (model:

130 IDS ui-3360cp-c-hq Rev.2) with a resolution of 2048x1088 pixels was also installed next to the lidar telescope to observe various types of surfaces. The image sampling rate was 1 Hz. Each picture incorporated the shooting time, and it provided a convenience to find the types of surfaces at different times. The photo name included the camera date and time, which was synchronized with the other instruments installed on the aircraft.

2.3.2 OCO-2 Dataset

135 The Orbiting Carbon observatory-2 (OCO-2), developed by NASA is the second satellite after the Greenhous gases Observing SATellite (GOSAT) to monitoring the CO_2 in the atmosphere to get a better understanding of the carbon cycle (Crisp, 2015; Crisp et al., 2008). The main objectives of the mission included measuring the atmospheric CO_2 with sufficient precision, accuracy and spatiotemporal resolution required to quantify the CO_2 sources and sinks at the regional and global scales. The sun-synchronous near-polar satellite included three high-resolution spectrometers making coincident measurements of the

140 reflected sunlight in the near-infrared CO_2 at 1.61 and 2.06 μm and oxygen at 0.76 μm (Wunch et al., 2017), In this study, OCO-2 XCO_2 version 10r Level 2 Lite product was used.

2.3.3 CarbonTracker Dataset

CarbonTracker is an inverse model framework developed by (Peters et al., 2005). It combines the two-way nested transfer model 5 (TM5) with offline Atmospheric Tracer transfer model and updates the atmospheric CO_2 distribution and surface

145 fluxes every year (Krol et al., 2004). It supports high-resolution data at regional level and coarse-resolution data at global scale. The Carbon Tracker provides the global CO_2 distribution at 25 pressure levels with a spatial grid resolution of 3°×2°

(Longitude/Latitude) and a temporal resolution of 3 hours (Babenhauserheide et al., 2015). The data product CTNRT2020 was used in this study (Jacobson et al., 2020).

2.4 IPDA Theory

150   The ACDL system developed for this study was based on two different wavelengths referred as the online and the offline wavelengths. The laser pulse of the online wavelength was strongly attenuated because it was absorbed by the trace gas molecules while propagating through the atmosphere. In contrast, the offline pulse was only weakly attenuated (Zhang et al., 2020). The online and offline wavelengths selected in this study were not affected by other molecules except CO_2. Because the online and the offline wavelengths were very close, the difference of scattering and absorption caused by the aerosols and

155   the gas molecules in the atmosphere could be ignored. Therefore, the difference between the two wavelength echo signals was mainly caused by atmospheric CO_2. The airborne IPDA lidar equation (Ehret et al., 2008; Refaat et al., 2016) is given in the following:

$$P_e(\lambda, R_A) = \eta_r \cdot O_r \frac{A}{(R_A - R_G)^2} \cdot \frac{E(\lambda)}{\Delta t(\lambda)} \cdot \rho^* \cdot T_m \cdot exp\left[-\tau_{CO_2}(\lambda, R_A)\right], \tag{1}$$

Where, P_e is the echo power, λ is the wavelength, η_r is the receiving optical efficiency, O_r is the overlap factor, A is the area

160   of the telescope, R_G is the height of the hard target above sea level, R_A is the altitude of the aircraft platform, E is the emission energy of the laser, Δt is the effective pulse width of the echo pulse, ρ^* is the target reflectivity, τ_{CO_2} is the two-way integral optical depth caused by the CO_2, and T_m is the atmospheric transmission efficiency. The detection signals of online and offline pulses are defined as $P_0(\lambda_{on})$ and $P_0(\lambda_{off})$, respectively. The echo signals of the online and offline pulses are $P(\lambda_{on}, R)$, and $P(\lambda_{off}, R)$, respectively. The IPDA single-pass Differential Absorption Optical Depth (DAOD) of the CO_2 can be expressed

165   as (Refaat et al., 2015):

$$\tau_{CO_2} = \int_{R_G}^{R_A} \Delta\sigma_{CO_2}\big(p(r), T(r)\big) N_{CO_2}(r)dr = \frac{1}{2} \cdot ln\left(\frac{P(\lambda_{off}, R) \cdot P_0(\lambda_{on})}{P(\lambda_{on}, R) \cdot P_0(\lambda_{off})}\right), \tag{2}$$

Where, $\Delta\sigma_{CO_2}$ is the differential absorption cross section of the online and offline wavelengths, N_{CO_2} is the molecular density of the CO_2, R_G is the height of the hard target above sea level, and R_A is the altitude of the aircraft platform. p and T are pressure and temperature profiles. When the APD detector receives the signal, it can convert the power into voltage using

170   equation 3 (Zhu et al., 2020):

$$V = P_P * \Re_v, \tag{3}$$

Where, $\Re_v$ represents the voltage response rate of the APD detector. Within the linear response range of the detector, the voltage response rate is a fixed value $\Re_v$ which the indicates signal power. Therefore, equation 2 can also be expressed as:

$$\tau_{CO_2} = \frac{1}{2} \cdot ln\left(\frac{V(\lambda_{off}, R) \cdot V_0(\lambda_{on})}{V(\lambda_{on}, R) \cdot V_0(\lambda_{off})}\right) \tag{4}$$

Where $V_0(\lambda_{on})$ and $V_0(\lambda_{off})$ are the detection signals voltage of online and offline pulses. $V(\lambda_{on}, R)$ and $V(\lambda_{off}, R)$ are the echo signals voltage of the online and offline pulses. For the airborne experiment, the vertical path XCO2 (in ppm) can be calculated the following equations:

$$X_{CO_2} = \frac{\tau_{CO_2}}{2 \times 10^{-6} \cdot IWF} , \tag{5}$$

$$IWF = \int_{R_G}^{R_A} \frac{N_A \cdot p(r) \cdot \Delta\sigma_{CO_2}(P(r), T(r))}{RT(r)(1 + X_{H_2O}(r))} dr , \tag{6}$$

Where, N_A is the Avogadro's constant, R is the gas constant, $P(r)$ and $T(r)$ are the pressure and temperature profiles, respectively. X_{H_2O} is the dry-air ratio of water vapor, IWF represents the integral weight function. IWF can be calculated using the temperature, pressure and humidity profiles obtained by the AIMMS and the High-resolution Transmission Molecular Absorption (HITRAN) database (Gordon et al., 2017).

3 Results and Discussion

3.1 Original Echo Signals

The performance of the ACDL system was evaluated by comparing the original echo signals over three different surface types, including the ocean, the mountain, and the urban residential areas. The original signals of the ACDL over the ocean, urban residential, and mountainous areas are shown in Figures 4, 5, and 6, respectively. The amplification signals from left to right are online monitor signal, online echo signal, offline monitor signal and offline echo signal. In each group of original echo signals, the monitoring signals are fixed at the same position but the echo signals appear in different positions due to the different heights of the target. The original signals were filtered before using, and signals whose pulse peak values were not in the linear region of APD were discarded. The echo signals in the ocean area were significantly smaller than those over the residential and the mountain areas. This might be due to the low reflectivity of the ocean, which leads to the reduction of the signal noise ratio (SNR) over the ocean. Moreover, no significant difference was observed between the echo signal strengths of residential and mountain areas.

3.2 Data Processing and Inversion Results

(Zhu et al., 2020) used the Matched Filter Algorithm (MFA) to extract the weak echo signals over the ocean in a previous research work. In addition, the differences between the Pulse Peak Method (PPM) and PIM were also compared while calculating the DAOD. The results showed that the SNR and accuracy of PIM were higher than those of the PPM. In this study, the PIM method was used to calculate the DAOD. The sum SNR was calculated using the following set of equations:

$$\rho^l = \frac{1}{N} \sum_{k=1}^{N} \alpha_k^l , \tag{7}$$

$$(\varepsilon^l)^2 = \frac{1}{N^2} \sum_{k=1}^{N} (\sigma_k^l)^2 , \tag{8}$$

$$SNR_{PIM}^l = \frac{\rho^l}{\varepsilon^l} = \frac{\sum_{k=1}^{N} \alpha_k^l}{\sqrt{\sum_{k=1}^{N}(\sigma_k^l)^2}}, \tag{9}$$

Where, N is the point number of the pulse, ρ^l and ε^l represent the mean and standard deviation. α_k^l is the value of each point on the pulse, and σ_k^l is the standard deviation of each point. We can increase the SNR of each pulse by accumulating the number of points on the pulse. Figure 7a shows the online wavelength monitoring signal, and figure 7b shows the change of SNR related to the number of accumulated points taken on the pulse. Figure 8a and 9a show the typical echo signals over the land and the ocean area. Figure 8b and 9b show the change of SNR related to the number of accumulated points taken on the pulse over different surface types. For the residential and mountain areas, the SNR was the highest when 5 points were taken before the pulse peak and 9 points were taken after the peak. And for the weak echo signal in the ocean area, when 7 points were taken before the pulse peak and 10 points were taken after the peak, the SNR was the largest.

The DAOD results calculated using the IPDA theory are shown in Figure 10. The DOAD values were smaller over the mountain area, however, no difference was found between the DAOD values of ocean and residential areas. The average DAOD values for mountain, ocean and residential areas were 0.44, 0.46, and 0.46, respectively. The results of the IWF and the XCO_2 calculated using equations 5 and 6 are shown in figures 11 and 12. The average values of the IWF over ocean, residential, and the mountainous areas are 1083.26, 1079.75, and 1037.05, respectively. In addition, the standard deviation of the IWF was the smallest for ocean surface and the largest for the mountainous area. The higher standard deviation for mountainous areas might be due to the fluctuations in height. Before retrieving the XCO_2, the aircraft attitude angle and the doppler shift were corrected using the inertial navigation data. The XCO_2 calculated from the ACDL measurements is shown in Figure 12. The XCO_2 is the largest over residential areas and the smallest over ocean. The largest XCO_2 over the urban residential areas might be attributed to the strong anthropogenic emissions (Mustafa et al., 2020), and the water body is generally a sink of the CO_2. The average values of XCO_2 over urban, oceanic, and mountainous areas were 430, 427.67, and 421.11 ppm, respectively. The distribution of XCO_2 on the flight trajectory and the surface photos captured using the installed coloured CMOS camera are shown in Figure 13.

3.3 In-Situ Measurement Results

Other data observed by airborne the ACDL are still being processed and analysed. In this study, the in-situ observations measured using the UGGA were also analysed for several days. The vertical profiles of the atmospheric CO_2 were measured using the UGGA during spiral and the descent of the aircraft and the results are shown in figure 14. The data recorded below 0.5 km were discarded because it produced errors and sudden spikes due to slowing down of the aircraft and the sudden pressure changes. Figure 14 shows that the atmospheric CO_2 concentration is the largest near the ground, and it decreases gradually with the progression in the altitude. This might be due to the weak photosynthesis as the plants are in dormant stage during winter in the northeast China (Mustafa et al., 2021). Moreover, the northeast China is also a source of carbon due to heating and industrial activities, which also contributes significantly to the atmospheric CO_2 (Shan et al., 1997). In addition,

the CO_2 concentration at different altitudes were the highest on 18 March. This could be caused by the weather conditions and pollution levels. Table 3 shows the weather report released by the Qinhuangdao meteorological station on each day of the flight.

Table 3: The weather report released by the Qinhuangdao Meteorological Department on each flight day.

Date Day Month	Weather	Temperature Highest / lowest	Wind direction/ Wind scale	AQI	PM2.5 (μg/m³)
11 March	sunny	16℃/ -3℃	Northeast/5	80	48
14 March	sunny	14℃/ -1℃	Northeast/3	60	28
16 March	cloudy	11℃/ -1℃	North/breeze	58	30
18 March	cloudy	10℃/ 4℃	Southwest/ breeze	175	131
19 March	cloudy	15℃/ 7℃	Southeast/1	139	105

The AOD values measured using various instruments on each flight day are shown Figure 15, and the results show that the AOD was the largest on 18 March. The highest CO_2 concentration on March 18 was likely to be caused by the higher pollution levels. A ground station was arranged in the flight area to verify the airborne results. The boundary layer height calculated using a Micro Pulse Lidar (MPL) installed at the Funing ground station on March 18 is shown in Figure 16. The dry-air mole fraction of CO_2 reaches its maximum value at about 1.4 km on March 18 (figure 14). This might be due to the fact that the height of the boundary layer was about 1.5 km on March 18 (figure 16), and the pollutants and the greenhouse gases cannot escape through the boundary layer.

Figure 17 shows the comparison of the XCO_2 calculated from the ACDL measurements with the dry-air mole fraction of CO_2 measured using the UGGA. Both of the datasets show a good agreement by exhibiting a similar variation trend. The results from the two datasets also show that the concentration of the atmospheric CO_2 is the highest over the residential area and the lowest over ocean surface. The average value of XCO_2 obtained by the ACDL calculations was 426.27 ppm, and the average value of CO_2 mole fraction obtained by the UGGA measurements was 413.91 ppm. Moreover, the standard deviation of the UGGA observations was relatively smaller than that of the ACDL measurements, and this might be due to the different working principles of the two instruments. The ACDL measures the weighted average concentrations at different altitudes. However, the UGGA measures the CO_2 value at the aircraft location.

3.4 OCO-2 Measurement Results

During this flight experiment, the OCO-2 passed over the flight area on March 16 and the observations over the study area are shown in Figure 18. OCO-2 observations covered both ocean and land surfaces. Due to the fast flight speed of the satellite, the data time period falling in the study area was from 12:57:25 to 12:57:38 UTC. A quality flag was applied to the satellite dataset and the cloud-contaminated retrievals were remove. The XCO_2 measured by OCO-2 varied from 401.66 ppm to 418.80 ppm, with an average of 414.25 ppm.

3.5 Vertical Profile Comparison of CO_2 Concentration

260 Figure 19 shows the vertical profile comparison of OCO-2, Carbon Tracker, and in-situ datasets. The CarbonTracker dataset was interpolated to the location of the experimental site. During the flight campaigns, the OCO-2 satellite passed over the flight area on March 16. Therefore, the data results of OCO-2 on March 16 were compared with those of CarbonTracker and in-situ data on March 14, March 16 and March 19, respectively. The structural change of CO_2 concentration with height can be roughly divided into two parts. From the ground to the height of 3 km and above 3 km. Below 3 km, the detection results

265 of OCO-2, UGGA and Carbon Tracker show a same decreasing result of CO_2 concentration value with the increase of altitude. When the altitude is more than 3 km, the CO_2 concentration is almost constant. Thig might be due to the stability of the upper atmosphere.

4 Conclusions

In this study, a 1.57 μm double-pulse airborne IPDA LIDAR was developed for atmospheric CO_2 monitoring. The airborne

270 experiment using the newly developed instrument was carried out during 11 - 19 March 2019 over Shanhaiguan, China. The IPDA LIDAR was installed on a research aircraft with some other instrument including a commercial CO_2 monitoring UGGA, an AIMMS, an INS, and a coloured CMOS camera. The flight path passed across various types of surfaces including the ocean, the mountain, and the residential areas. From the original signals obtained by the IPDA LIDAR, the echo signals over the ocean area were relatively smaller than those over the mountain and the residential areas. In order to process the echo signal

275 with low SNR over the ocean, PIM method was used to calculate DAOD. By calculating the SNR of the detection signal of online wavelength, we determined that when 6 points were taken before the pulse peak and 7 points after the peak, the SNR was the largest. For the residential and mountain areas, the SNR was the highest when 5 points were taken before the pulse peak and 9 points were taken after the peak. And for the weak echo signal over the ocean area, when 7 points were taken before the pulse peak and 10 points were taken after the peak, the SNR was the largest. The data obtained by airborne IPDA LIDAR

280 on March 14 was processed and analysed. The results showed that the XCO_2 over the ocean surface was the smallest, with an average value of 421.11ppm, and that was the largest over residential area with an average value of 430 ppm. The average XCO_2 value over the mountainous area was 427.67 ppm. Moreover, the dry-air mole fraction of CO_2 measured by UGGA was also analysed for several days and the results showed that the CO_2 concentration was the largest on 18 March, that was the most polluted day during the entire flight campaign. The UGGA CO_2 concentration was compared with the XCO_2 calculated

285 using the IPDA LIDAR measurements, and both of the datasets showed a good agreement by exhibiting a similar variation trend. In addition, the vertical profiles of CO_2 were also measured using UGGA and compared with OCO-2 and the Carbon Tracker CO_2 datasets. All the datasets showed a similar variation result with some differences in their concentrations. The CO_2 concentration from the Carbon Tracker was relatively larger than the dry-air mole fraction of CO_2 measured using the UGGA. The atmospheric CO_2 concentration was the highest near the ground and it decreased gradually with the progression in the

290 altitude.

Author contributions. QW and SZZ did the flight experiment, and QW processed the data results. FM provided the satellite and mode data and analysis methods, and FM modified the grammar and format of the whole article. LBB guided the writing of manuscripts. JQL and WBC JQL guided the flight experiment.

295

Competing interests. The authors declare that they have no conflict of interest.

Acknowledgments. The authors acknowledge the support of the Shanghai Institute of Satellite Engineering for conducting the experiment. The authors thank the Funing Meteorological Bureau for providing a ground station for the experiment. The

300 authors acknowledge the efforts of NASA to provide the OCO-2 data products. These data were produced by the OCO-2 project at the Jet Propulsion Laboratory, California Institute of Technology, and obtained from the OCO-2 data archive maintained at the NASA Goddard Earth Science Data and Information Services Center. The authors also acknowledge NOAA Earth System Research Laboratory for their data products. The 2nd author (Farhan Mustafa) is highly grateful to the China Scholarship Council (CSC) and the NUIST for granting the fellowship and providing the required supports.

305

Financial support. This research has been supported the National Natural Science Foundation of China (NSFC) (41675133).

References

Abshire, J., Ramanathan, A., Riris, H., Mao, J., Allan, G., Hasselbrack, W., Weaver, C. and Browell, E.: Airborne Measurements of CO_2 Column Concentration and Range Using a Pulsed Direct-Detection IPDA Lidar, Remote Sens., 6(1),

310 443–469, doi:10.3390/rs6010443, 2013.

Abshire, J. B., Ramanathan, A. K., Riris, H., Allan, G. R., Sun, X., Hasselbrack, W. E., Mao, J., Wu, S., Chen, J., Numata, K., Kawa, S. R., Yang, M. Y. M. and DiGangi, J.: Airborne measurements of CO<sub>2</sub> column concentrations made with a pulsed IPDA lidar using a multiple-wavelength-locked laser and HgCdTe APD detector, Atmos. Meas. Tech., 11(4), 2001–2025, doi:10.5194/amt-11-2001-2018, 2018.

315 Amediek, A., Ehret, G., Fix, A., Wirth, M., Büdenbender, C., Quatrevalet, M., Kiemle, C. and Gerbig, C.: CHARM-F—a new airborne integrated-path differential-absorption lidar for carbon dioxide and methane observations: measurement performance and quantification of strong point source emissions, Appl. Opt., 56(18), 5182, doi:10.1364/AO.56.005182, 2017.

Araki, M., Morino, I., MacHida, T., Sawa, Y., Matsueda, H., Ohyama, H., Yokota, T. and Uchino, O.: CO_2 column-averaged volume mixing ratio derived over Tsukuba from measurements by commercial airlines, Atmos. Chem. Phys., 10(16), 7659–

320 7667, doi:10.5194/acp-10-7659-2010, 2010.

Babenhauserheide, A., Basu, S., Houweling, S., Peters, W. and Butz, A.: Comparing the CarbonTracker and TM5-4DVar data assimilation systems for CO 2 surface flux inversions, , 9747–9763, doi:10.5194/acp-15-9747-2015, 2015.

Baer, D. S., Paul, J. B., Gupta, M. and O'Keefe, A.: Sensitive absorption measurements in the near-infrared region using off-axis integrated-cavity-output spectroscopy, Appl. Phys. B, 75(2), 261–265, doi:10.1007/s00340-002-0971-z, 2002.

325 Ballantyne, A. P., Alden, C. B., Miller, J. B., Trans, P. P. and White, J. W. C.: Increase in observed net carbon dioxide uptake by land and oceans during the past 50 years, Nature, 488(7409), 70–73, doi:10.1038/nature11299, 2012.

Crisp, D.: Measuring atmospheric carbon dioxide from space with the Orbiting Carbon Observatory-2 (OCO-2), in Proc.SPIE, vol. 9607., 2015.

Crisp, D., Miller, C. E. and DeCola, P. L.: NASA Orbiting Carbon Observatory: measuring the column averaged carbon

330 dioxide mole fraction from space, J. Appl. Remote Sens., 2(1), 1–14, doi:10.1117/1.2898457, 2008.

Crisp, D., Fisher, B. M., O'Dell, C., Frankenberg, C., Basilio, R., Bösch, H., Brown, L. R., Castano, R., Connor, B., Deutscher, N. M., Eldering, A., Griffith, D., Gunson, M., Kuze, A., Mandrake, L., McDuffie, J., Messerschmidt, J., Miller, C. E., Morino, I., Natraj, V., Notholt, J., O'Brien, D. M., Oyafuso, F., Polonsky, I., Robinson, J., Salawitch, R., Sherlock, V., Smyth, M., Suto, H., Taylor, T. E., Thompson, D. R., Wennberg, P. O., Wunch, D. and Yung, Y. L.: The ACOS CO 2 retrieval algorithm

335 - Part II: Global XCO$_2$ data characterization, Atmos. Meas. Tech., 5(4), 687–707, doi:10.5194/amt-5-687-2012, 2012.

Dlugokencky Ed, T. P.: Trends in Atmospheric Carbon Dioxide, Noaa/Esrl, http://www.esrl.noaa.gov/gmd/ccgg/trends/global.ht [online] Available from: ftp://aftp.cmdl.noaa.gov/products/trends/co2/co2_mm_gl.txt (Accessed 3 May 2020), 2016.

Du, J., Zhu, Y., Li, S., Zhang, J., Sun, Y., Zang, H., Liu, D., Ma, X., Bi, D., Liu, J., Zhu, X. and Chen, W.: Double-pulse 157

340 μm integrated path differential absorption lidar ground validation for atmospheric carbon dioxide measurement, Appl. Opt., 56(25), 7053, doi:10.1364/AO.56.007053, 2017.

Ehret, G., Kiemle, C., Wirth, M., Amediek, A., Fix, A. and Houweling, S.: Space-borne remote sensing of CO_2, CH_4, and N_2O by integrated path differential absorption lidar: a sensitivity analysis, Appl. Phys. B, 90(3–4), 593–608, doi:10.1007/s00340-007-2892-3, 2008.

345 Gong, Y., Bu, L., Yang, B. and Mustafa, F.: High Repetition Rate Mid-Infrared Differential Absorption Lidar for Atmospheric Pollution Detection, Sensors, 20(8), 2211, doi:10.3390/s20082211, 2020.

Gordon, I. E., Rothman, L. S., Hill, C., Kochanov, R. V., Tan, Y., Bernath, P. F., Birk, M., Boudon, V., Campargue, A., Chance, K. V., Drouin, B. J., Flaud, J.-M., Gamache, R. R., Hodges, J. T., Jacquemart, D., Perevalov, V. I., Perrin, A., Shine, K. P., Smith, M.-A. H., Tennyson, J., Toon, G. C., Tran, H., Tyuterev, V. G., Barbe, A., Császár, A. G., Devi, V. M., Furtenbacher,

350 T., Harrison, J. J., Hartmann, J.-M., Jolly, A., Johnson, T. J., Karman, T., Kleiner, I., Kyuberis, A. A., Loos, J., Lyulin, O. M., Massie, S. T., Mikhailenko, S. N., Moazzen-Ahmadi, N., Müller, H. S. P., Naumenko, O. V., Nikitin, A. V., Polyansky, O. L., Rey, M., Rotger, M., Sharpe, S. W., Sung, K., Starikova, E., Tashkun, S. A., Auwera, J. Vander, Wagner, G., Wilzewski, J., Wcisło, P., Yu, S. and Zak, E. J.: The HITRAN2016 molecular spectroscopic database, J. Quant. Spectrosc. Radiat. Transf., 203, 3–69, doi:10.1016/j.jqsrt.2017.06.038, 2017.

355 Hedelius, J. K., Parker, H., Wunch, D., Roehl, C. M., Viatte, C., Newman, S., Toon, G. C., Podolske, J. R., Hillyard, P. W., Iraci, L. T., Dubey, M. K. and Wennberg, P. O.: Intercomparability of XCO$_2$ and XCH$_4$ from the United States TCCON sites,

Atmos. Meas. Tech., 10(4), 1481–1493, doi:10.5194/amt-10-1481-2017, 2017.

Hungershoefer, K., Peylin, P., Chevallier, F., Rayner, P., Klonecki, A., Houweling, S. and Marshall, J.: Evaluation of various observing systems for the global monitoring of CO2 surface fluxes, Atmos. Chem. Phys., 10(21), 10503–10520,

360   doi:10.5194/acp-10-10503-2010, 2010.

Jacobson, A. R., Schuldt, K. N., Miller, J. B., Tans, P., Andrews, A., Mund, J., Aalto, T., Bakwin, P., Bergamaschi, P., Biraud, S. C., Chen, H., Colomb, A., Conil, S., Cristofanelli, P., Davis, K., Delmotte, M., DiGangi, J. P., Dlugokencky, E., Emmenegger, L., Fischer, M. L., Hatakka, J., Heliasz, M., Hermanssen, O., Holst, J., Jaffe, D., Karion, A., Keronen, P., Kominkova, K., Kubistin, D., Laurent, O., Laurila, T., Lee, J., Lehner, I., Leuenberger, M., Lindauer, M., Löfvenius, M. O.,

365   Lopez, M., Mammarella, I., Manca, G., Marek, M. V, Marklund, P., Martin, M. Y., McKain, K., Miller, C. E., Mölder, M., Myhre, C. L., Pichon, J. M., Plass-Dölmer, C., Ramonet, M., Scheeren, B., Schumacher, M., Sloop, C. D., Steinbacher, M., Sweeney, C., Thoning, K., Tørseth, K., Turnbull, J., Viner, B., Vitkova, G., Wekker, S. De, Weyrauch, D. and Worthy, D.: CarbonTracker Near Real-Time, CT-NRT.v2020-1, , doi:10.25925/RCHH-MS75, 2020.

Kawa, S. R., Mao, J., Abshire, J. B., Collatz, G. J., Sun, X. and Weaver, C. J.: Simulation studies for a space-based CO 2 lidar

370   mission, Tellus B Chem. Phys. Meteorol., 62(5), 759–769, doi:10.1111/j.1600-0889.2010.00486.x, 2010.

Kiel, M., Dell, C. W. O., Fisher, B., Eldering, A., Nassar, R., Macdonald, C. G. and Wennberg, P. O.: How bias correction goes wrong : measurement of X CO 2 affected by erroneous surface pressure estimates, , 2241–2259, 2019.

Kong, Y., Chen, B. and Measho, S.: Spatio-temporal consistency evaluation of XCO$_2$ retrievals from GOSAT and OCO-2 based on TCCON and model data for joint utilization in carbon cycle research, Atmosphere (Basel)., 10(7), 1–23,

375   doi:10.3390/atmos10070354, 2019.

Krol, M., Houweling, S., Bregman, B., van den Broek, M., Segers, A., van Velthoven, P., Peters, W., Dentener, F. and Bergamaschi, P.: The two-way nested global chemistry-transport zoom model TM5: algorithm and applications, Atmos. Chem. Phys. Discuss., 4(4), 3975–4018, doi:10.5194/acpd-4-3975-2004, 2004.

Kulawik, S., Wunch, D., Dell, C. O., Frankenberg, C., Reuter, M., Oda, T., Chevallier, F., Sherlock, V., Buchwitz, M.,

380   Osterman, G., Miller, C. E., Wennberg, P. O., Griffith, D., Morino, I., Dubey, M. K., Deutscher, N. M., Notholt, J., Hase, F., Warneke, T., Sussmann, R., Robinson, J., Strong, K., Schneider, M., Mazière, M. De, Shiomi, K., Feist, D. G., Iraci, L. T., Wolf, J., Environm, A. and Inst, R.: Consistent evaluation of ACOS-GOSAT , BESD-SCIAMACHY , CarbonTracker , and MACC through comparisons to TCCON, , 683–709, doi:10.5194/amt-9-683-2016, 2016.

Lei, L., Zhong, H., He, Z., Cai, B., Yang, S., Wu, C., Zeng, Z., Liu, L. and Zhang, B.: Assessment of atmospheric CO$_2$

385   concentration enhancement from anthropogenic emissions based on satellite observations, Kexue Tongbao/Chinese Sci. Bull., 62(25), 2941–2950, doi:10.1360/N972016-01316, 2017.

Liang, A., Gong, W., Han, G. and Xiang, C.: Comparison of satellite-observed XCO$_2$ from GOSAT, OCO-2, and ground-based TCCON, Remote Sens., 9(10), 1–26, doi:10.3390/rs9101033, 2017.

Lindqvist, H., O'Dell, C. W., Basu, S., Boesch, H., Chevallier, F., Deutscher, N., Feng, L., Fisher, B., Hase, F., Inoue, M.,

390   Kivi, R., Morino, I., Palmer, P. I., Parker, R., Schneider, M., Sussmann, R. and Yoshida, Y.: Does GOSAT capture the true

seasonal cycle of carbon dioxide?, Atmos. Chem. Phys., 15(22), 13023–13040, doi:10.5194/acp-15-13023-2015, 2015.

Mao, J., Ramanathan, A., Abshire, J. B., Kawa, S. R., Riris, H., Allan, G. R., Rodriguez, M., Hasselbrack, W. E., Sun, X., Numata, K., Chen, J., Choi, Y. and Yang, M. Y. M.: Airborne lidar reflectance measurements at 1.57 mu m in support of the A-SCOPE mission for atmospheric CO_2, Atmos. Meas. Tech., 11(1), 127–140, doi:10.5194/amt-11-127-2018, 2018a.

395   Mao, J., Ramanathan, A., Abshire, J. B., Kawa, S. R., Riris, H., Allan, G. R., Rodriguez, M., Hasselbrack, W. E., Sun, X., Numata, K., Chen, J., Choi, Y. and Yang, M. Y. M.: Measurement of atmospheric CO_2 column concentrations to cloud tops with a pulsed multi-wavelength airborne lidar, Atmos. Meas. Tech., 11(1), 127–140, doi:10.5194/amt-11-127-2018, 2018b.

Mendonca, J., Strong, K., Wunch, D., Toon, G. C., Long, D. A., Hodges, J. T., Sironneau, V. T. and Franklin, J. E.: Using a speed-dependent Voigt line shape to retrieve O 2 from Total Carbon Column Observing Network solar spectra to improve

400   measurements of XCO 2, Atmos. Meas. Tech., 12(1), 35–50, doi:10.5194/amt-12-35-2019, 2019.

Mustafa, F., Bu, L., Wang, Q., Ali, M. A., Bilal, M., Shahzaman, M. and Qiu, Z.: Multi-year comparison of CO_2 concentration from NOAA carbon tracker reanalysis model with data from GOSAT and OCO-2 over Asia, Remote Sens., 12(15), doi:10.3390/RS12152498, 2020.

Mustafa, F., Wang, H., Bu, L., Wang, Q., Shahzaman, M., Bilal, M., Zhou, M., Iqbal, R., Aslam, R. W., Ali, M. A. and Qiu,

405   Z.: Validation of GOSAT and OCO-2 against In Situ Aircraft Measurements and Comparison with CarbonTracker and GEOS-Chem over Qinhuangdao, China, Remote Sens., 13(5), 899, doi:10.3390/rs13050899, 2021.

O'Dell, C. W., Connor, B., Bösch, H., O'Brien, D., Frankenberg, C., Castano, R., Christi, M., Eldering, D., Fisher, B., Gunson, M., McDuffie, J., Miller, C. E., Natraj, V., Oyafuso, F., Polonsky, I., Smyth, M., Taylor, T., Toon, G. C., Wennberg, P. O. and Wunch, D.: The ACOS CO_2 retrieval algorithm-Part 1: Description and validation against synthetic observations, Atmos. Meas.

410   Tech., 5(1), 99–121, doi:10.5194/amt-5-99-2012, 2012.

Paul, J. B., Lapson, L. and Anderson, J. G.: Ultrasensitive absorption spectroscopy with a high-finesse optical cavity and off-axis alignment, Appl. Opt., 40(27), 4904–4910, doi:10.1364/AO.40.004904, 2001.

Peters, W., Miller, J. B., Whitaker, J., Denning, A. S., Hirsch, A., Krol, M. C., Zupanski, D., Bruhwiler, L. and Tans, P. P.: An ensemble data assimilation system to estimate CO_2 surface fluxes from atmospheric trace gas observations, J. Geophys. Res.

415   Atmos., 110(D24), doi:10.1029/2005JD006157, 2005.

Refaat, T. F., Singh, U. N., Yu, J., Petros, M., Ismail, S., Kavaya, M. J. and Davis, K. J.: Evaluation of an airborne triple-pulsed 2 μm IPDA lidar for simultaneous and independent atmospheric water vapor and carbon dioxide measurements, Appl. Opt., 54(6), 1387, doi:10.1364/AO.54.001387, 2015.

Refaat, T. F., Singh, U. N., Yu, J., Petros, M., Remus, R. and Ismail, S.: Double-pulse 2-μm integrated path differential

420   absorption lidar airborne validation for atmospheric carbon dioxide measurement, Appl. Opt., 55(15), 4232, doi:10.1364/AO.55.004232, 2016.

Santer, B. D., Painter, J. F., Bonfils, C., Mears, C. A., Solomon, S., Wigley, T. M. L., Gleckler, P. J., Schmidt, G. A., Doutriaux, C., Gillett, N. P., Taylor, K. E., Thorne, P. W. and Wentz, F. J.: Human and natural influences on the changing thermal structure of the atmosphere, Proc. Natl. Acad. Sci. U. S. A., 110(43), 17235–17240, doi:10.1073/pnas.1305332110, 2013.

425 Schultz, M. G., Akimoto, H., Bottenheim, J., Buchmann, B., Galbally, I. E., Gilge, S., Helmig, D., Koide, H., Lewis, A. C., Novelli, P. C., Plass-Dölmer, C., Ryerson, T. B., Steinbacher, M., Steinbrecher, R., Tarasova, O., Tørseth, K., Thouret, V. and Zellweger, C.: The global atmosphere watch reactive gases measurement network, Elementa, 3, 1–23, doi:10.12952/journal.elementa.000067, 2015.

Shan, Y., Guan, D., Zheng, H., Ou, J., Li, Y., Meng, J., Mi, Z., Liu, Z. and Zhang, Q.: China CO_2 emission accounts 1997-
430 2015, Sci. Data, 1–14 [online] Available from: www.nature.com/sdata/, 1997.

Stocker, B. D., Roth, R., Joos, F., Spahni, R., Steinacher, M., Zaehle, S., Bouwman, L., Xu-Ri and Prentice, I. C.: Multiple greenhouse-gas feedbacks from the land biosphere under future climate change scenarios, Nat. Clim. Chang., 3(7), 666–672, doi:10.1038/nclimate1864, 2013.

Sun, X., Duan, M., Gao, Y., Han, R., Ji, D., Zhang, W., Chen, N., Xia, X., Liu, H. and Huo, Y.: In situ measurement of CO_2
435 and CH4 from aircraft over northeast China and comparison with OCO-2 data, Atmos. Meas. Tech., 13(7), 3595–3607, doi:10.5194/amt-13-3595-2020, 2020.

UNFCC: Paris Agreement., 2015.

Wunch, D., Wennberg, P. O., Osterman, G., Fisher, B., Naylor, B., Roehl, M. C., O'Dell, C., Mandrake, L., Viatte, C., Kiel, M., Griffith, D. W. T., Deutscher, N. M., Velazco, V. A., Notholt, J., Warneke, T., Petri, C., De Maziere, M., Sha, M. K.,
440 Sussmann, R., Rettinger, M., Pollard, D., Robinson, J., Morino, I., Uchino, O., Hase, F., Blumenstock, T., Feist, D. G., Arnold, S. G., Strong, K., Mendonca, J., Kivi, R., Heikkinen, P., Iraci, L., Podolske, J., Hillyard, P., Kawakami, S., Dubey, M. K., Parker, H. A., Sepulveda, E., García, O. E., Te, Y., Jeseck, P., Gunson, M. R., Crisp, D. and Eldering, A.: Comparisons of the Orbiting Carbon Observatory-2 (OCO-2) XCO_2 measurements with TCCON, Atmos. Meas. Tech., 10(6), 2209–2238, doi:10.5194/amt-10-2209-2017, 2017.

445 Xie, J., Huang, X., Bu, L., Zhang, H., Mustafa, F. and Chu, C.: Detection of water cloud microphysical properties using multi-scattering polarization lidar, Curr. Opt. Photonics, 4(3), 174–185, doi:10.3807/COPP.2020.4.3.174, 2020.

Yang, S., Lei, L., Zeng, Z., He, Z. and Zhong, H.: An Assessment of Anthropogenic CO_2 Emissions by Satellite-Based Observations in China, Sensors (Basel)., 19(5), 1118, doi:10.3390/s19051118, 2019.

Yokota, T., Yoshida, Y., Eguchi, N., Ota, Y., Tanaka, T., Watanabe, H. and Maksyutov, S.: Global Concentrations of CO 2
450 and CH 4 Retrieved from GOSAT : First Preliminary Results, , 5, 160–163, 2009.

Yu, J., Petros, M., Singh, U. N., Refaat, T. F., Reithmaier, K., Remus, R. G. and Johnson, W.: An Airborne 2-μm Double-Pulsed Direct-Detection Lidar Instrument for Atmospheric CO_2 Column Measurements, J. Atmos. Ocean. Technol., 34(2), 385–400, doi:10.1175/JTECH-D-16-0112.1, 2017.

Zhang, X., Wang, F., Wang, W., Huang, F., Chen, B., Gao, L., Wang, S., Yan, H., Ye, H., Si, F., Hong, J., Li, X., Cao, Q.,
455 Che, H. and Li, Z.: The development and application of satellite remote sensing for atmospheric compositions in China, Atmos. Res., 245, 105056, doi:10.1016/j.atmosres.2020.105056, 2020.

Zhu, Y., Yang, J., Chen, X., Zhu, X., Zhang, J., Li, S., Sun, Y., Hou, X., Bi, D., Bu, L., Zhang, Y., Liu, J. and Chen, W.: Airborne Validation Experiment of 1.57-μm Double-Pulse IPDA LIDAR for Atmospheric Carbon Dioxide Measurement,

Remote Sens., 12(12), 1999, doi:10.3390/rs12121999, 2020.

460
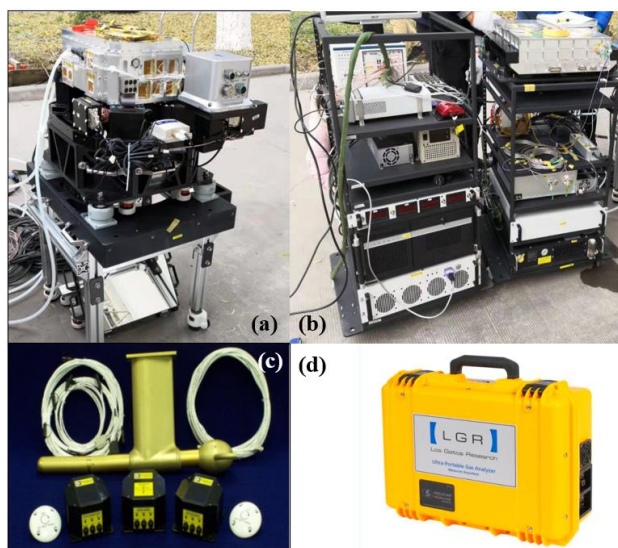
Figure 1: The physical picture of IPDA lidar system. (a) It is the transceiver system, installed in the pod outside the aircraft. (b) It is the control system and data acquisition system of some equipment, which is installed in the sealed cabin of the aircraft. (c) It is the the Aircraft Integrated Meteorological Measurement System (AIMMS). (d) It is a commercial instrument Ultraportable Greenhouse
465 **Gas Analyzer, that was installed in an unsealed cabin of the aircraft.**
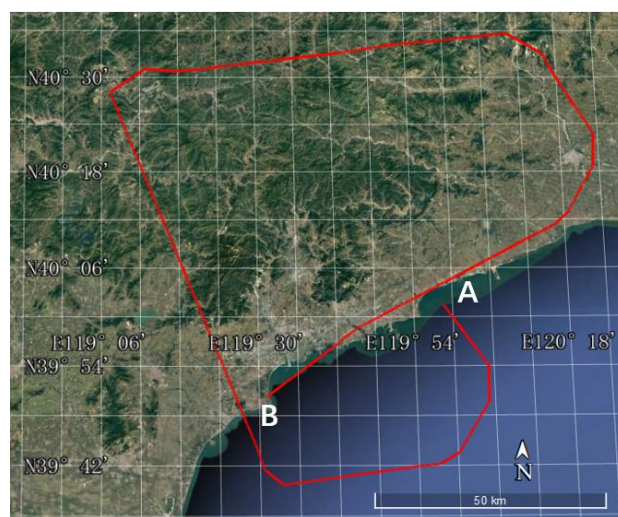
Figure 2: Flight trajectory of the flight on 14 March 2019. The starting point of the flight was A, and the ending point was B (© Google Earth Pro).

470
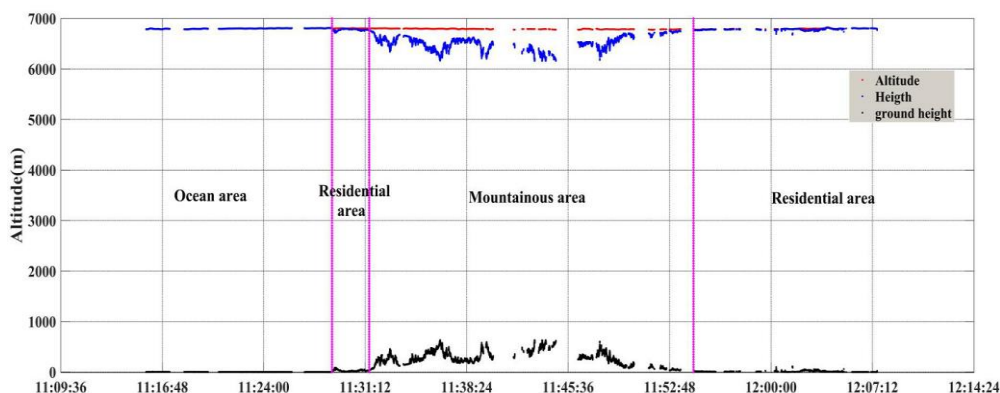
Figure 3: Aircraft flight height and corresponding surface elevation on 14 March 2019. The red dots are the altitude of the aircraft measured by the onboard GPS system. The blue scatter points are the distance measured by lidar. The black scattered points are the difference between the altitude measured by the GPS and the distance measured by the lidar, and also represent the surface
475 **elevation. The purple-red vertical line is the dividing line of different surface types.**
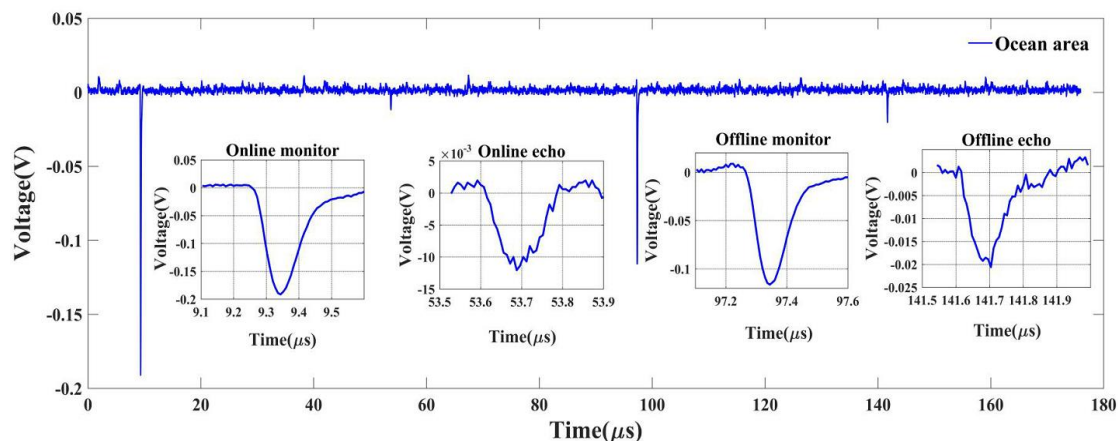
Figure 4: Original echo signal of ocean area (total signal and pulse amplification signal). The amplification signals from left to right are online monitor signal, online echo signal, offline monitor signal and offline echo signal.

480
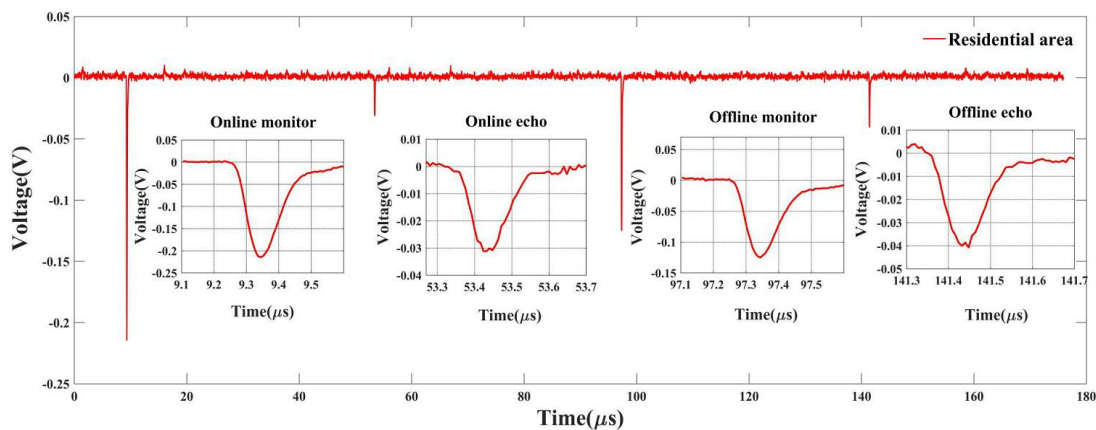
Figure 5: Original echo signal of urban residential area (total signal and pulse amplification signal). The amplification signals from left to right are online monitor signal, online echo signal, offline monitor signal and offline echo signal.

485
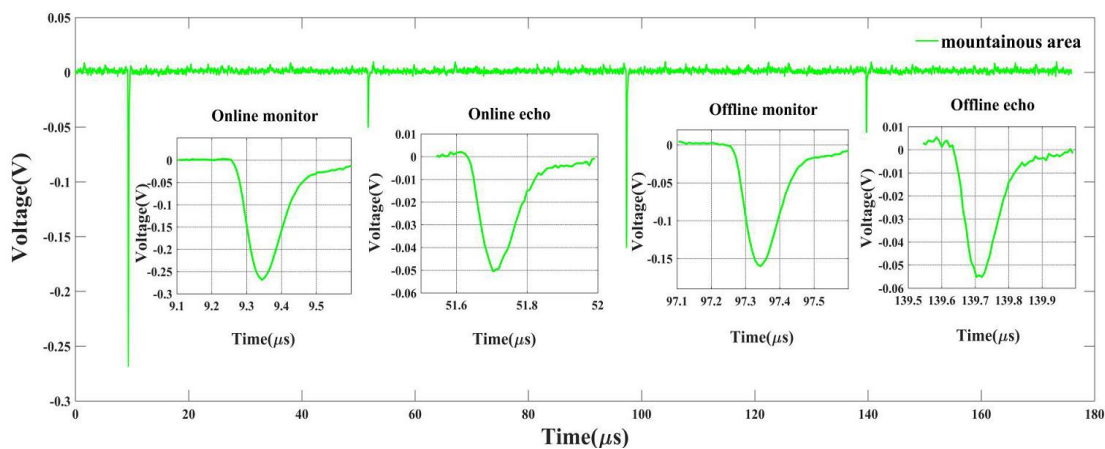
Figure 6: Original echo signal of mountain area (total signal and pulse amplification signal). The amplification signals from left to right are online monitor signal, online echo signal, offline monitor signal and offline echo signal.
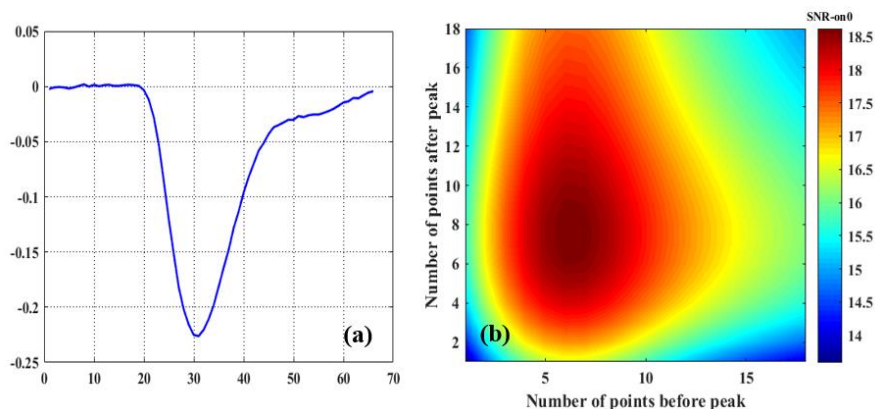
490 **Figure 7: (a) Online wavelength monitoring pulse signal. (b) The change of pulse signal SNR with the number of selected pulse points.**
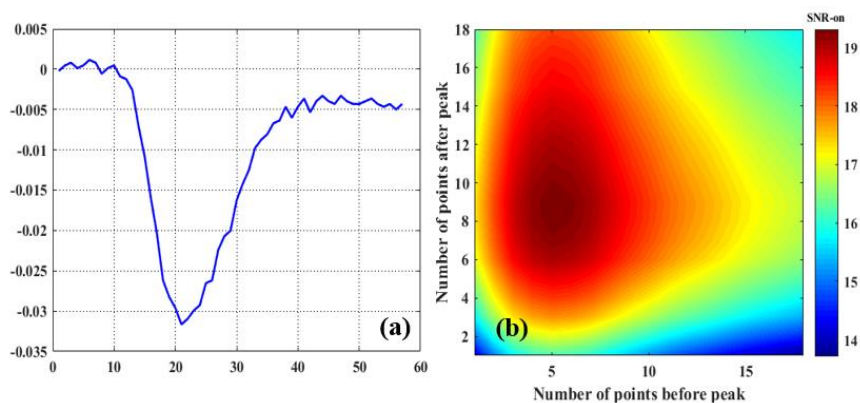
Figure 8: (a) Online wavelength echo pulse signal in land area. (b) The change of the SNR of the echo pulse signal in the land area with the number of selected pulse points.
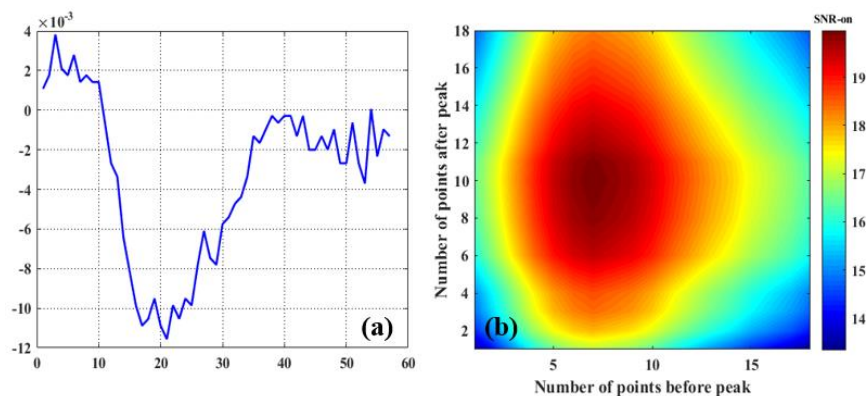
495

Figure 9: (a) Online wavelength echo pulse signal in ocean area. (b) The change of the SNR of the echo pulse signal in the ocean area with the number of selected pulse points.
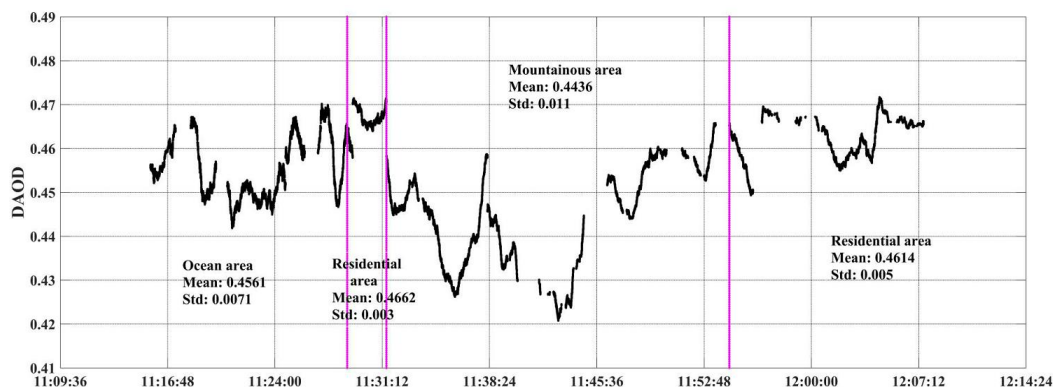
Figure 10: DAOD results in ocean areas, urban residential areas and mountain areas on 14 March 2019. The purplish red vertical line represents the boundary of different surface types. The plane passes through the ocean area, urban residential area, mountain area and urban residential area in turn, which is the same in the following results.
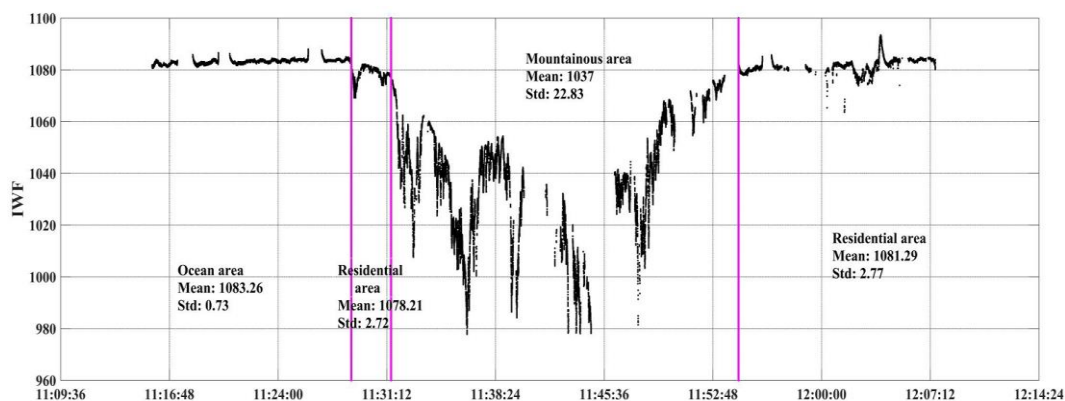
Figure 11: IWF results in ocean, urban residential and mountainous areas on 14 March 2019. The purplish red vertical line represents the boundary of different surface types. The plane passes through the ocean area, urban residential area, mountain area and urban residential area in turn.
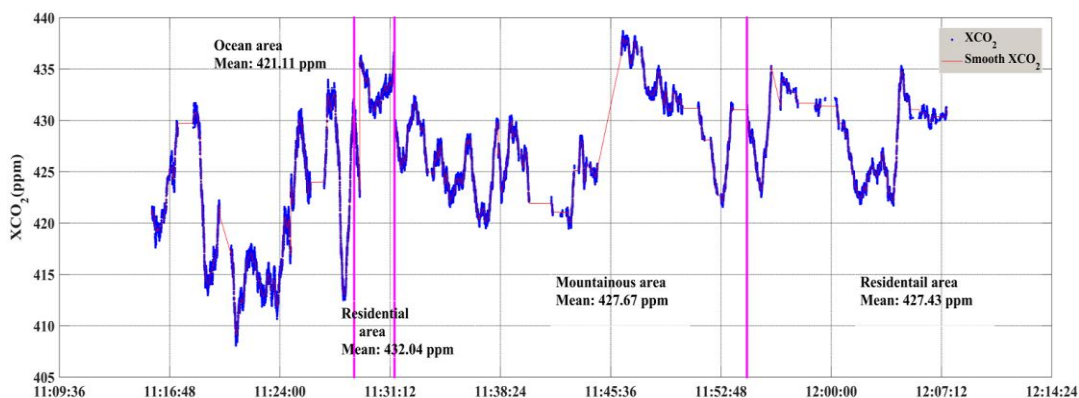
Figure 12: XCO₂ results in ocean, urban residential and mountainous areas on 14 March 2019. The purplish red vertical line represents the boundary of different surface types. The plane passes through the ocean area, urban residential area, mountain area and urban residential area in turn.
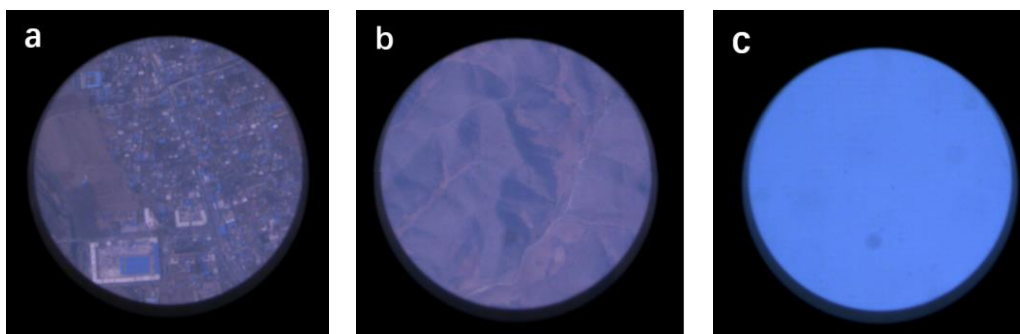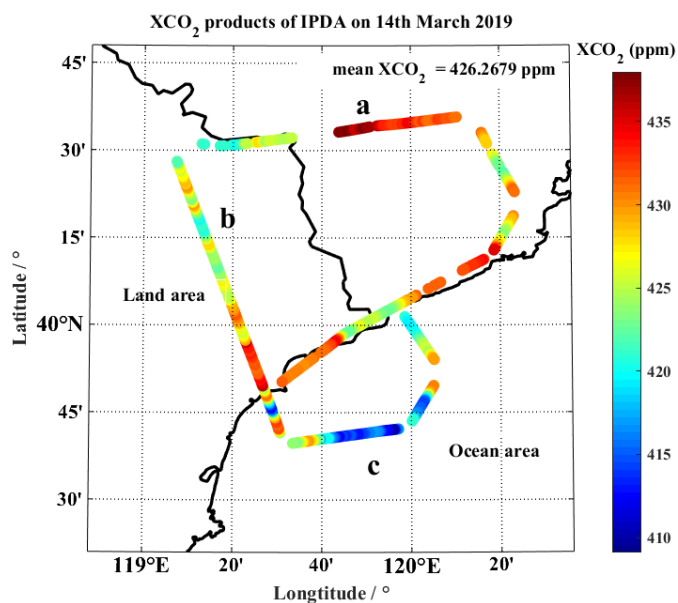
Figure 13: XCO₂ distribution on the flight trajectory and surface photos of typical areas on 14 March 2019. Among them, a represents the urban residential area, b represents the mountain area, and c represents the ocean area.

515
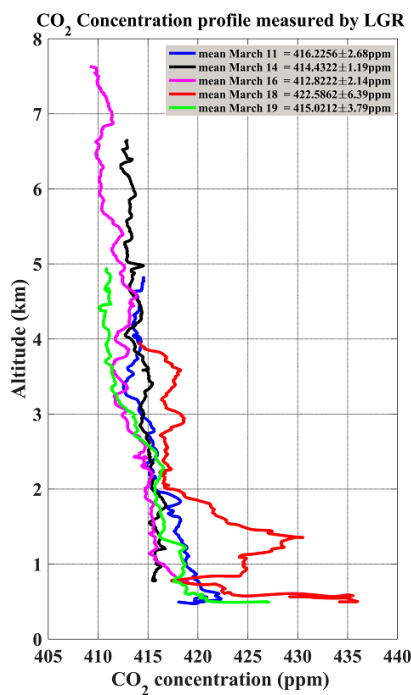
Figure 14: CO₂ concentration profile results measured by greenhouse gas analyzer during aircraft descending flight on different dates. The blue solid line is the result on March 11. The black solid line is the result of March 14. The purple solid line is the result of March 16. The solid red line is the result of March 18. The green solid line is the result of March 19.

520
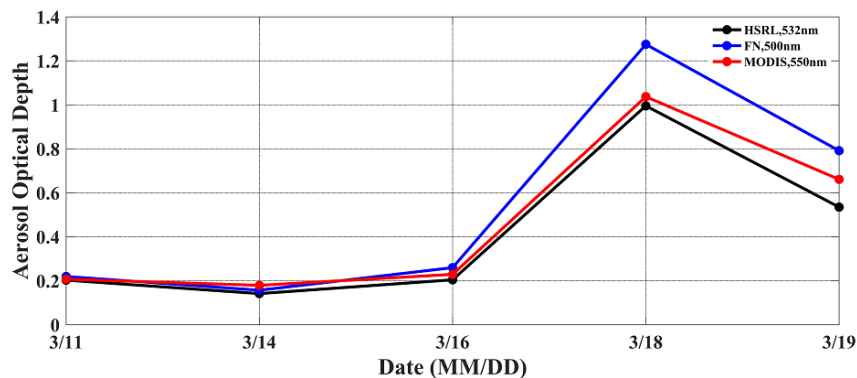
Figure 15: Aerosol optical depth results on different dates. The blue scatter is measured by the sun photometer of Funing ground station. The black scatter is the measurement results of the airborne lidar 532nm channel. The red scattered points are the measurement results of Moderate Resolution Imaging Spectroradiometer (MODIS)

525
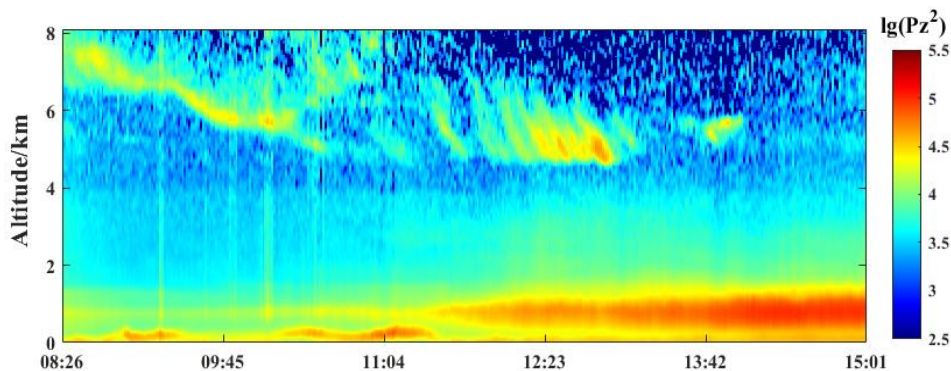
Figure 16: MPL measurement results of Funing ground station on March 18.
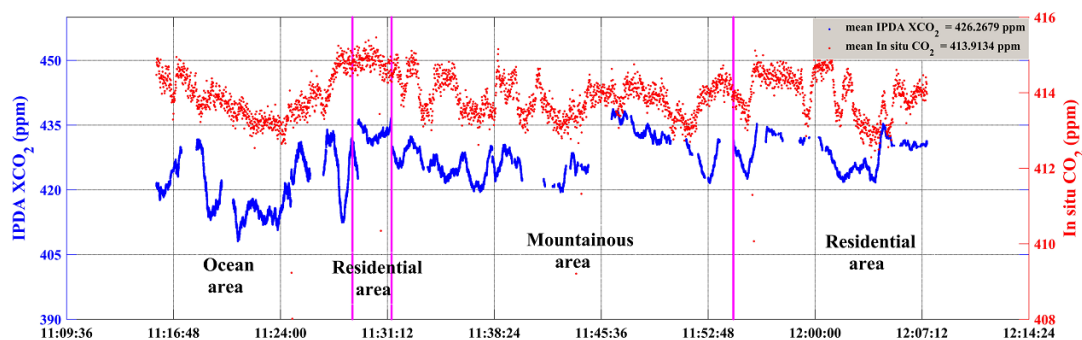
530 **Figure 17: XCO₂ comparison results of airborne IPDA lidar and LGR on 14 March 2019. The red scatter is the result of greenhouse gas analyzer. The blue scatter is measured by airborne IPDA lidar. The purplish red vertical line represents the boundary of different surface types. The plane passes through the ocean area, urban residential area, mountain area and urban residential area in turn.**

535
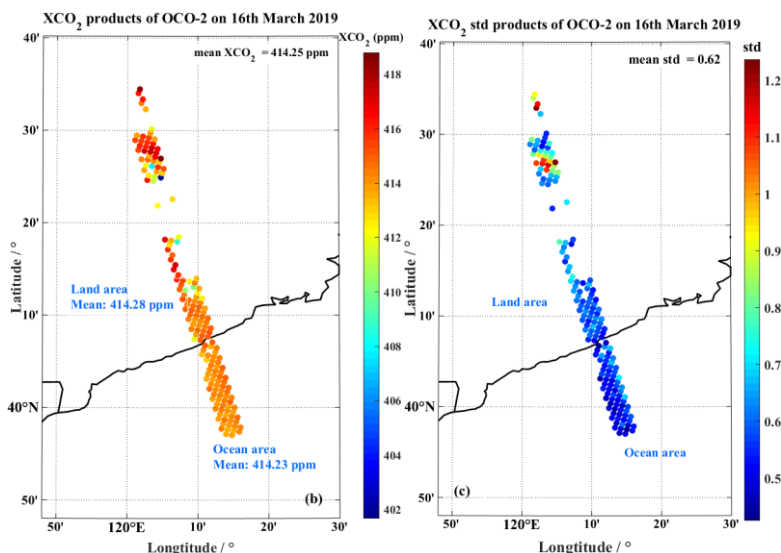
Figure 18: Orbit and detection results of OCO-2 satellite on March 16. The solid red line in figure (a) is the flight path of the aircraft. The yellow mark point is the position of the suborbital point of the OCO-2 trajectory in the flight area (© Google Earth Pro). Figure (b) shows the XCO₂ results detected by OCO-2. Figure (c) shows the corresponding standard deviation.

540
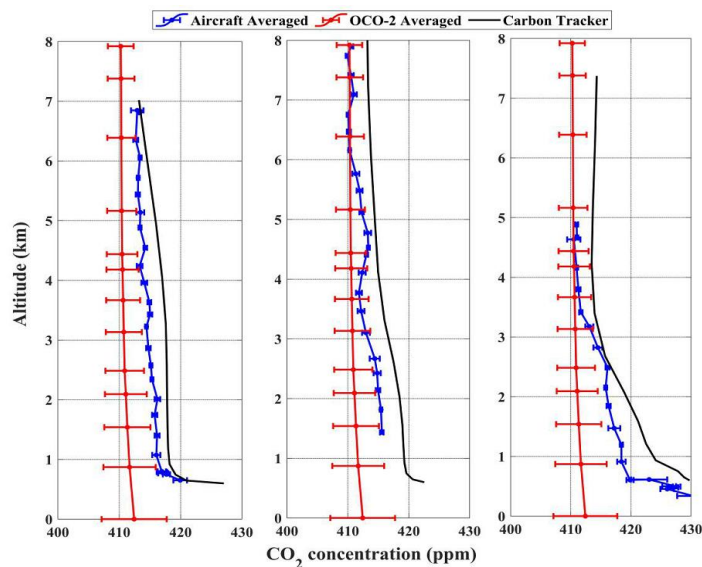
Figure 19: CO₂ concentration profile comparison results of airborne greenhouse gas analyzer and OCO-2 satellite, CT model. Figure (a) is the vertical structure of CO₂ concentration on March 14. Figure (b) shows the vertical structure of CO₂ concentration on March 16. Figure (c) shows the vertical structure of CO₂ concentration on March 19. The red scatter is the inversion result of OCO-2. The blue scatter is the measurement result of the airborne greenhouse gas analyzer. The black solid line is the result of CT model.

545